AGU PUBLICATIONS

JGR

Journal of Geophysical Research: Solid Earth

RESEARCH ARTICLE

10.1002/2014JB011270

Key Points:
- Imaging of a Pacific mid-ocean ridge transform fault (RTF) zone
- Correlation between the material properties and the mechanical behavior
- Importance of damaged fault zones in the mechanical behavior of RTFs

Correspondence to:
B. Froment,
fromentb@mit.edu

Citation:
Froment, B., J. J. McGuire, R. D. van der Hilst, P. Gouédard, E. C. Roland, H. Zhang, and J. A. Collins (2014), Imaging along-strike variations in mechanical properties of the Gofar transform fault, East Pacific Rise, *J. Geophys. Res. Solid Earth*, *119*, 7175–7194, doi:10.1002/2014JB011270.

Received 9 MAY 2014
Accepted 18 AUG 2014
Accepted article online 22 AUG 2014
Published online 23 SEP 2014

Imaging along-strike variations in mechanical properties of the Gofar transform fault, East Pacific Rise

B. Froment[1], J. J. McGuire[2], R. D. van der Hilst[1], P. Gouédard[1,3], E. C. Roland[2,4], H. Zhang[5], and J. A. Collins[2]

[1]Department of Earth, Atmospheric, and Planetary Sciences, Massachusetts Institute of Technology, Cambridge, Massachusetts, USA, [2]Department of Geology and Geophysics, Woods Hole Oceanographic Institution, Woods Hole, Massachusetts, USA, [3]Now at Magnitude LLC, Sainte-Tulle, France, [4]USGS Alaska Science Center, Anchorage, Alaska, USA, [5]School of Earth and Space Sciences and Geophysical Research Institute, University of Science and Technology of China, Hefei,China

Abstract A large part of global plate motion on mid-ocean ridge transform faults (RTFs) is not accommodated as major earthquakes. When large earthquakes do occur, they often repeat quasiperiodically. We focus here on the high slip rate (~14 cm/yr) Gofar transform fault on the equatorial East Pacific Rise. This fault is subdivided into patches that slip during M_w 5.5–6 earthquakes every 5 to 6 years. These patches are separated by rupture barriers that accommodate slip through swarms of smaller events and/or aseismic creep. We performed an imaging study to investigate which spatiotemporal variations of the fault zone properties control this segmentation in mechanical behavior and could explain the specific behavior of RTFs at the global scale. We adopt a double-difference approach in a joint inversion of active air gun shots and microseismicity recorded for 1 year. This data set includes the 2008 M_w 6 Gofar earthquake. The along-strike *P* wave velocity structure reveals an abrupt transition between the barrier area, characterized by a damaged fault zone of 10–20% reduced V_p and a nearly intact fault zone in the asperity area. The importance of the strength of the damage zone on the mechanical behavior is supported by the temporal *S* wave velocity changes which suggest increased damage within the barrier area, during the week preceding the M_w 6 earthquake. Our results support the conclusion that extended highly damaged zones are the key factor in limiting the role of major earthquakes to accommodate plate motion along RTFs.

1. Introduction

Understanding how slip is accommodated on faults is critical for developing a comprehensive model of the seismic cycle. Several processes exist in the spectrum of fault slip behavior from steady aseismic creep to major ordinary earthquakes, including slow and silent earthquakes, nonvolcanic tremors, and swarms of small earthquakes [e.g., *Beroza and Ide*, 2011]. Understanding how these stress release processes contribute to fault slip is important for anticipating earthquake behavior and, thus, for hazard assessment.

Mid-ocean ridge transform faults (RTFs) are generally poorly coupled, that is, a large part of global plate motion on RTFs is accommodated aseismically [*Brune*, 1968; *Bird et al.*, 2002; *Boettcher and Jordan*, 2004]. Recent studies have shown that Pacific RTFs consist of segments with low coupling separated by patches that are fully coupled [e.g., *McGuire*, 2008; *Sykes and Ekström*, 2012], but the underlying mechanisms controlling these different behaviors in accommodating strain are still poorly understood. In this paper we investigate the influence of material properties and fault structure on RTF mechanical behavior.

For several reasons, RTFs represent an attractive tectonic environment for fault mechanics studies because they are relatively simple in comparison to continental faults. They tend to occur as single, long-lived faults (rather than branching, distributed fault systems found in continental crust), with average slip rates well defined by plate spreading velocities. Furthermore, oceanic lithosphere has a more homogeneous composition, and its thermal structure is more predictable (from known plate kinematics). The behavior of RTFs may, therefore, be less dependent on geologic history than continental fault systems. In addition, East Pacific Rise RTFs present short and well-defined seismic cycles [*McGuire*, 2008; *Boettcher and McGuire*, 2009], leading to a tectonic context particularly adapted for studies of the seismic cycle. RTFs may be considered as a simple fault configuration whose study can provide insights into fault mechanics in general.

©2014. American Geophysical Union. All Rights Reserved.

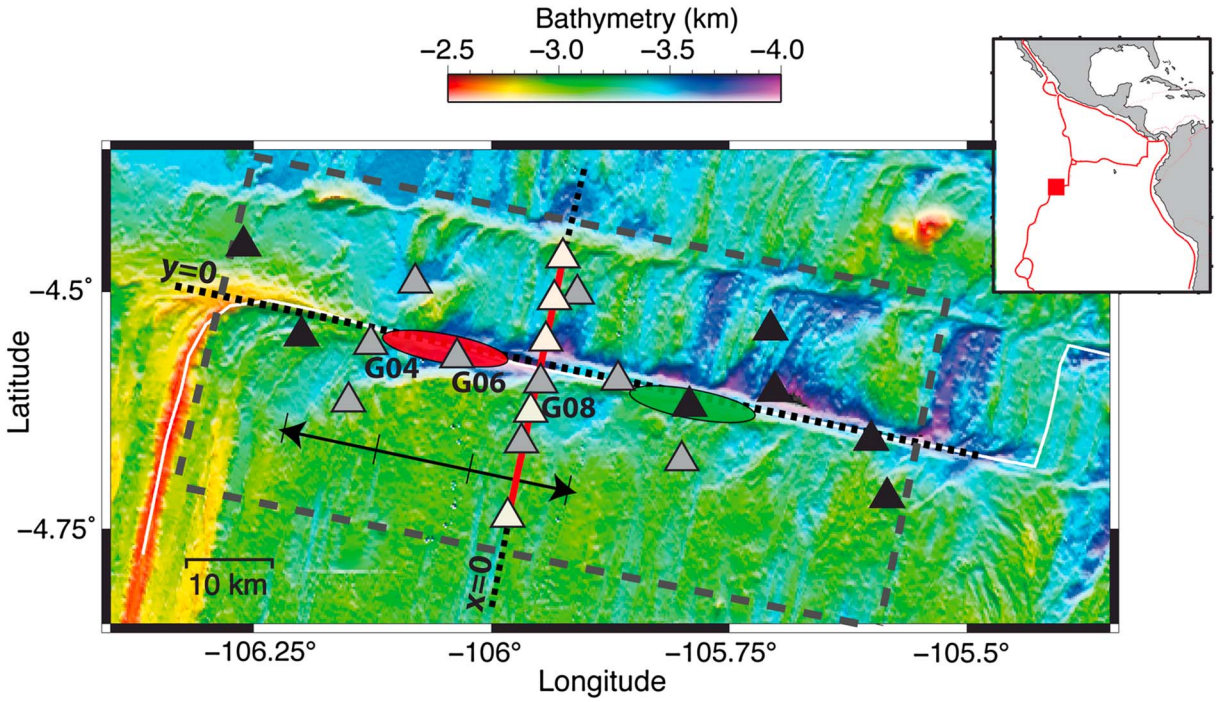

Figure 1. Bathymetry map with geographical location indicated by the red square on the inset. Black and gray triangles stand for the ocean bottom seismographs (OBSs) deployed for 1 year in 2008 that recorded the microseismicity. White triangles stand for OBSs deployed during the active source experiment. The red line shows the location of the 100 m spaced active sources considered in this study. Gray and white triangles correspond to OBSs of both experiments that recorded active source shots. The location of OBSs G04, G06, and G08 is indicated as these stations are used as reference points throughout the paper. The red and green ellipses are centered on the 2008 M_w 6.0 and 2007 M_w 6.2 earthquakes, respectively, and indicate two main asperities that break every 5 to 6 years [*McGuire*, 2008]. The dark gray dashed rectangle outlines the region parameterized in the inversion, and the two black dashed lines show our local coordinate system, centered on the G08 OBS, with the *x* and *y* axes positive to the east and north, respectively. The black arrow indicates the along-strike range that our study focused on, and the ticks point out the segmentation described in section 3.2.

We focus here on the short (~90 km), high slip rate (~14 cm/yr) Gofar transform fault on the equatorial East Pacific Rise (EPR). This fault is subdivided into multiple patches that slip during magnitude 5.5–6 earthquakes roughly every 5 years [*McGuire*, 2008; *Boettcher and McGuire*, 2009]. The red and green ellipses in Figure 1 point out 15 km long patches that ruptured in 1997, 2002, 2008, 2013, and in 1996, 2002, 2007, and 2012. The 15 km length has been estimated from the distribution of the 2008 aftershocks, which can however slightly overestimate the rupture lengths. The patches generating moderate to large earthquakes are separated by stationary rupture barriers that prevent ruptures from connecting multiple patches despite the quasi-synchronization of their seismic cycles [*McGuire*, 2008; *Boettcher and McGuire*, 2009]. Instead, these barrier regions may accommodate plate motion through swarms of smaller events, transient or continuous (aseismic) creep, or both [*McGuire et al.*, 2012; *Roland and McGuire*, 2009].

Motivated by the regularity of EPR seismic cycles, the Woods Hole Oceanographic Institution (WHOI) conducted a large seismic experiment at the Gofar transform fault in 2008. Two data sets were collected. First, an active source, wide-angle refraction line was acquired across the fault (red line in Figure 1). This data set was used by *Roland et al.* [2012] to build a high-resolution image of the *P* wave velocity variations within the central rupture barrier segment of the Gofar fault. They found a few-kilometer-wide zone of reduced V_p (~10–20%) around the active fault that extends throughout the crust. WHOI also deployed an array of 16 broadband ocean bottom seismographs (OBSs) around the Gofar fault, which recorded ground motion continuously throughout 2008 (black and gray triangles in Figure 1). This network captured the 18 September 2008 M_w 6.0 Gofar earthquake as well as its foreshocks and aftershocks, providing a data set covering times both early and late in the seismic cycles of individual segments. *McGuire et al.* [2012] used this data set to analyze a swarm of about 20,000 foreshocks confined to the same central rupture barrier segment as the one imaged by *Roland et al.* [2012]. Their observations point to enhanced fluid circulation in that fault area. In this paper we combine the two data sets to perform a 3-D inversion and build an along-strike image of the elastic structure, thereby extending our material characterization across the different fault segments.

©2014. American Geophysical Union. All Rights Reserved.

Previous seismic studies of the crustal structure of RTFs reported low *P* wave velocities near fault zones [e.g., *Tréhu and Purdy*, 1984; *Detrick et al.*, 1993; *Van Avendonk et al.*, 1998, 2001], interpreted as evidence for intense fracturing and hydrothermal alteration associated with strike-slip motion along active faults. These studies, however, focused on geologic processes that control fault morphology and not on relationships between material properties and earthquake processes. *Roland et al.* [2012] were the first to look at this slow anomaly in terms of earthquake behavior and suggested that the extension of the low-velocity damage zone throughout the crust could explain the absence of moderate to large earthquakes in the central part of the Gofar fault. This hypothesis is supported by *Van Avendonk et al.* [1998, 2001] who reported evidence for relatively intact gabbro within the seismogenic zone of the Clipperton transform fault (at 10°N on the EPR) that generates large earthquakes and has high seismic coupling [*Boettcher and Jordan*, 2004]. However, these studies involved different fault systems and the different behaviors could have several explanations. The 3-D approach adopted here on the Gofar fault, which shows a clear segmentation in mechanical behavior, presents a unique opportunity to establish unambiguously the relationship between material properties of the fault zone and seismic behavior.

2. Tomographic Method

We adopt a double-difference approach that uses both absolute and differential arrival times in a joint inversion for event location and velocity structure [*Zhang and Thurber*, 2003], which gives more accurate results than tomographic inversion of absolute arrival times alone. Indeed, the double-difference method takes advantage both of the higher accuracy of the differential time data and the restriction of corresponding sensitivity kernels to the source region.

An earthquake catalog covering the calendar year of 2008 was constructed using standard short-term average to long-term average (STA/LTA)-based detection algorithms for *P* and *S* wave arrival times. We then selected earthquakes with at least 14 arrivals from the catalog and event pairs linked by more than eight phase pairs. Significant connectedness between events helps stabilize the solution [*Waldhauser and Ellsworth*, 2000, 2002]. A total of 7644 earthquakes remained. In addition to these passive data, we use 271 air gun shots, that is, the portion of the above mentioned active source data set that falls into our model space (red line in Figure 1). *P* wave first arrivals from these active shots were picked by hand on five OBSs deployed during the active experiment (beige triangles in Figure 1) and on nine of the 1 year OBSs deployed within 20 km of the air gun line (gray triangles in Figure 1). Picks were made in similar frequency ranges for the two data sets: 3–15 Hz for the active source data and 5–15 Hz for the passive source (microseismicity) STA-LTA detection.

We applied different confidence-based weights to the *P* wave arrival times to combine both data sets. The (manually picked) active shot arrival times from nearby stations are generally of high quality, but phase picking for the more distant OBSs proved to be more challenging. To account for the difference in reliability, we applied weights between 0.5 (for the distant OBSs) and 1 (nearby OBSs) to arrivals from active shots. *P* wave arrivals detected through the STA-LTA procedure are considered reliable but associated with a lower weight than the best manual picks (0.9).

Three types of data are used in the inversions: absolute *P* wave arrival times from both active shots and earthquakes, catalog *P* and *S* wave differential arrival times, and *P* and *S* wave differential arrival times computed by waveform cross correlation (WCC) between pairs of earthquakes [*Waldhauser and Ellsworth*, 2000; *Zhang and Thurber*, 2003]. Following *Zhang and Thurber* [2003], we combine these data by applying a hierarchical weighting scheme. We first apply greater weight to absolute *P* arrival times in order to constrain long-wavelength structures. In subsequent stages we increase the weight of the catalog and WCC differential times in order to refine event locations and velocity structures near the source region. Appendix A shows the weighting scheme as well as the evolution of the travel time residuals and hypocenter parameters during the inversion process. We note that in view of the lower quality of automatic *S* wave first-arrival picks, we do not use *S* wave absolute arrival times, except to test their effect on the depth extent of the relocated seismicity (in section 5).

We think that the *S* wave STA-LTA-detected arrivals can still be useful in the overall iteration process. Picking errors can be random or systematic. The effect of random errors may increase through the differencing process, but systematic errors will be suppressed [*Zhang and Thurber*, 2006]. We thus use the *S* wave differential times to better constrain the inversion. To deal with random errors in differential *S* wave arrival times

©2014. American Geophysical Union. All Rights Reserved.

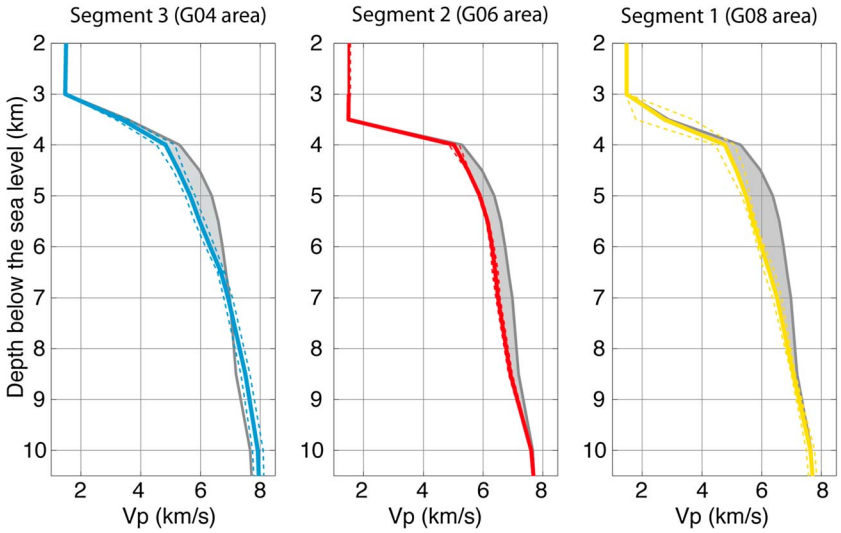

Figure 2. One-dimensional velocity-depth profiles for the (left, middle, and right) three defined segments (colored lines). These models correspond to the average of the *P* wave velocity model in each segment. Note that this figure shows the average in the center of each segment, i.e., leaving out the transition areas observed in the along-strike V_p models (Figure B2 in Appendix B). In practice, the average has been made over three across-fault nodes by 4, 2, and 3 along-strike nodes for segments 1, 2, and 3, respectively. The dashed lines delimit the range of mean ±1 standard deviation. The gray-shaded area highlights the difference with the starting model (gray line), representing normal EPR crust.

derived from the first arrival picks (the so-called catalog differential times), we (1) remove outliers and (2) apply a lower weight to *S* wave times compared to *P* wave times (see Table A1). As WCC differential times do not depend on the STA-LTA picks, *S* and *P* waves are weighted similarly for this type of data.

The final data input is composed of 42,947 *P* wave absolute arrival times, 336,568 *P* wave and 392,237 *S* wave catalog differential times, and 39,759 *P* wave and 37,384 *S* wave WCC differential times. We perform our inversions in a discretized 85 km long, 25 km wide, and 25 km deep model space in a coordinate system rotated 12° to approximately fault-parallel (x) and fault-normal (y) axes (black dashed lines in Figure 1). In the internal part of our inversion grid, $dx = 3$ km, $dy = 1$ km, and $dz = 0.5$ km. We use the TomoDD code, based on a damped least squares solver [*Zhang and Thurber*, 2003, 2006] for the simultaneous determination of event locations and wave speed variations. We invert for both *P* and *S* wave velocity models. We use an average of the V_p model obtained by *Roland et al.* [2012] outside the Gofar fault zone, representing normal EPR crust, as the 1-D starting model, and a V_p/V_s ratio of 1.73. Finally, we integrated seafloor bathymetry to build a crustal starting model for our inversion.

We note that the source/receiver geometry is not ideal for a 3-D tomography. Receivers are located along a line following the fault, plus another line perpendicular to it for the duration of the active experiment. Source locations follow a similar pattern, with the background seismicity located along the fault, plus a line of active sources perpendicular to it. This is sufficient, however, to characterize differences in medium properties in the barrier and asperity fault zones, which is the objective of this work.

3. Velocity Structure

3.1. Results

Figure 2 shows the 1-D V_p structure of the fault zone on three segments in the western part of the fault (between $x = 6$ km and $x = -25$ km, see the black arrow in Figure 1). The models displayed correspond to the *P* wave velocity structure averaged between $y = -0.5$ km and $y = 2.5$ km (with positive y indicating north of the main fault). This 3 km wide fault zone is centered around the low-velocity zone mapped by *Roland et al.* [2012]. Segment 1 (between $x = 6$ km and $x = -6$ km) coincides with the long-term rupture barrier identified by *McGuire et al.* [2012]. This area is characterized by a strong low-velocity anomaly relative to the starting model, displayed in gray in Figure 2. The fault zone velocity is up to 20% less than the average *P* wave velocity in nearby oceanic crust (Figure 2, right). This result is in good agreement with the 2-D velocity model for that area built by *Roland et al.* [2012] using *P* wave absolute travel times from just

©2014. American Geophysical Union. All Rights Reserved.

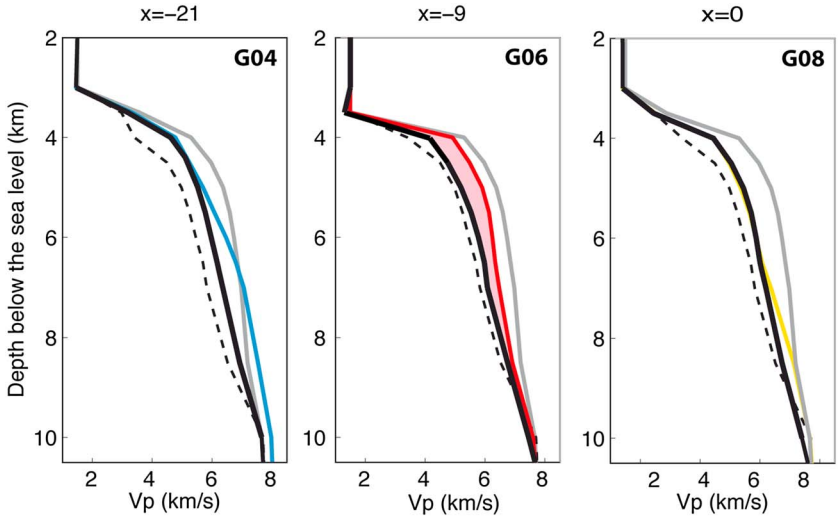

Figure 3. (left, middle, right) Results of the synthetic tests, similar to Figure 2. The black dashed line shows the input model used to build synthetic data, that is, the model obtained by *Roland et al.* [2012]. The gray curve represents the starting model in the synthetic tests (note that it is the same as we used in the real data inversion). The black solid line shows the recovered model after inversion of synthetic data. For comparison, the model obtained by inverting real data (shown in Figure 2) is plotted as the colored lines. The pink-shaded area in the middle panel highlights the difference between the synthetic data model and the real data one in segment 2. This difference confirms that our model brings out a structure around G06 that is resolvably faster than the model found by *Roland et al.* [2012] in segment 1 (e.g., under G08).

the active source data set. Our combined data set reveals that this low-velocity anomaly fades westward to reach significantly higher *P* wave velocities in a segment comprising the 2008 M_w 6.0 earthquake epicenter area (between $x = -6$ km and $x = -15$ km, Figure 2, middle). In segment 3, farther west ($x = -15$ km to $x = -25$ km), V_p decreases again in the upper crust (Figure 2 left), but the anomaly extends less deep than in segment 1 (~3.5 km compared to ~5.5 km). Seismometers G08, G06, and G04 are located in segments 1, 2, and 3, respectively, and will thus be used as reference point for each segment (Figure 1). This along strike variability in the strength of the low-velocity zone is the first-order result of our model. Appendix B presents the whole range of along-strike 1-D V_p profiles that have been used to identify these three segments as well as vertical slices of the model across and along the fault.

3.2. Resolution Tests

The along-strike range across which our model can be considered reliable is defined using test inversions with synthetic data. For this purpose, we generate a synthetic model by laterally extending the 2-D *P* wave velocity model obtained by *Roland et al.* [2012]. We thus impose a low-velocity fault zone all along the fault (black dashed lines in Figure 3). From this model, we create synthetic travel time data for the source and receiver pairs used in our study, which are then inverted in the same way as the recorded data and using the same starting model, representing normal EPR crust (gray curve in Figures 2 and 3). The resulting model is displayed as black solid lines in Figure 3. We used this test to determine the region of our model that is well constrained by our data (Appendix B). Figure B1 shows that the structure in the eastern part of the fault is less well constrained, and we decided to focus on the range between $x = -25$ km and $x = 6$ km (black arrow in Figure 1).

We also utilize this synthetic experiment to make sure that the faster structure revealed by our model near the 2008 M_w 6 earthquake is not an artifact due to poor ray coverage. Figure 3 compares our real data V_p model to the synthetic tests in the three areas of interest. First, the comparison between the synthetic data model (black solid line) and the input model (black dashed line) in this figure gives an idea of the impact of the ray coverage on our inversion. In particular, the synthetic tests imply that the model slightly overestimates velocity everywhere. The ray coverage thus limits our ability to fully retrieve the actual model from the relatively high-velocity starting model. In segment 1 (Figure 3, right) the excellent agreement between the real data model (yellow line) and the synthetic data model (black solid line) confirms that the structure revealed by our model in this area is similar within the uncertainty caused by ray coverage to the input

©2014. American Geophysical Union. All Rights Reserved.

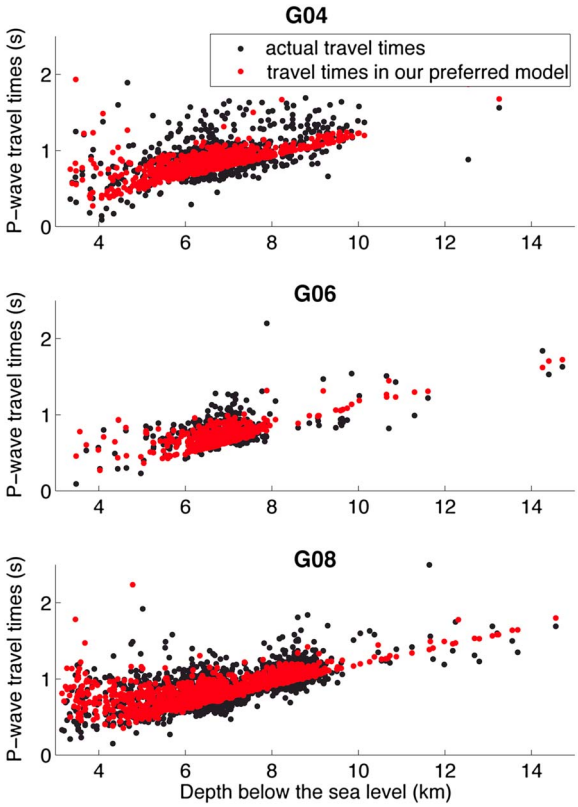

Figure 4. STA-LTA-detected *P* wave travel times from microseismicity data (black dots) and *P* wave travel times predicted by our preferred model (red dots) at station (top) G04, (middle) G06, and (bottom) G08 for events located beneath each of the stations. Note that some earthquakes are clearly located deeper than the main bulk of seismicity and may not be reliable.

model used to generate synthetic data, that is, the low-velocity model obtained by *Roland et al.* [2012]. Results in the western segment (Figure 3, left) suggest that structures closer to the edge of our network are not well resolved, since the black solid line is farther away from the black dashed line. However, the reasonable agreement between the model obtained (blue line) and the results of the synthetic tests (black solid line) in the first ~2.5 km of the crust suggest that this region may contain the same slow anomaly, but our data set does not resolve it completely. The velocity structure in the western segment may thus be slower than our model prediction. By contrast, the difference between the real data model and the synthetic data one in the deeper crust, supports the idea that the slow anomaly would actually be shallower than in segment 1. Following the same argument, the clear difference between the real data model and the synthetic data one in segment 2, highlighted by the pink-shaded area in Figure 3 (middle) confirms that the difference between segments 1 and 2 is not a bias due to poor coverage and the faster structure revealed by our model within the M_w 6 rupture zone must reflect an actual higher velocity region.

We further evaluate the reliability of our model by examining its ability to predict the observed *P* wave travel times from the active and passive data sets. Figure 4 shows the comparison between the automatic STA-LTA *P* wave travel times detected on the passive data set (black dots) and the *P* wave travel times expected in our preferred model (red dots) as a function of event depth. For each station (G04, G06, and G08) we selected events located within ±3 km of the station in the along-strike direction. We observe that our model explains the overall features of the *P* wave microseismic data well. However, the larger discrepancies at G04 reflect again the difficulties in resolving structural and hypocentral parameters close to the edge of the network. We note that some earthquakes are located deeper than the main bulk of seismicity and may not be reliable. However, we were hesitant to reject these events in the inversion process based on their depth, since the depth extension of the seismicity remains open (see discussion in section 5).

Active source data are particularly useful to investigate the accuracy of our *P* wave velocity model because (1) the active shot travel time data are picked by hand and therefore may be more accurate than STA-LTA picks and, most importantly, (2) there is no ambiguity on the source locations allowing a straightforward interpretation of travel times in terms of velocity structure. We will revisit this point later. Figure 5 shows a comparison between the observed (black dots) and the predicted times from both the starting model (gray crosses) and our preferred model (colored dots) for stations G04, G06, G08, and G09. This highlights both the fit in the along-strike direction (on the three segments represented by G04, G06, and G08) and along the perpendicular active source line (G08 and G09).

We first notice the significant improvement provided by our model in terms of fitting the data. The fit at G09 is better than at G08, which may be due to the fact that rays traveling from southern (warm color) sources to G09 turn in the mid-to-lower crust and sample the core of the low-velocity fault zone, whereas rays from shots recorded at G08 (located right on top of the fault zone) do not. Our model also does a fairly good job explaining the data within the asperity area (G06). These results indicate that the transition between segments 1 and 2 is well represented by our model. As expected from its more remote location, we observe

©2014. American Geophysical Union. All Rights Reserved.

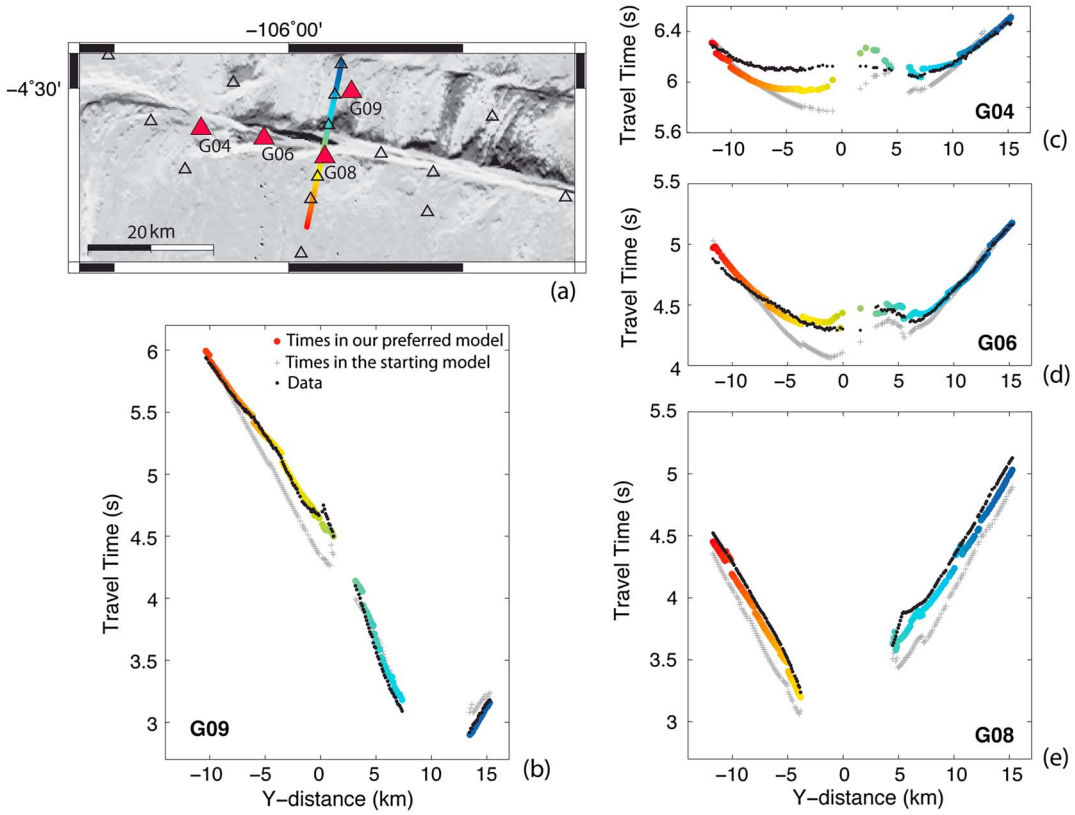

Figure 5. (a) Location map of the active sources (colored dots) and the stations examined (red triangles). Comparison of hand-picked *P* wave travel times (black dots), travel times predicted by our preferred model (colored dots), and predicted by the 1-D starting model representing normal EPR crust (gray crosses) at (b) G09, (c) G04, (d) G06, and (e) G08. The scale is the same for all plots. Color only indicates the location of the shots. Negative *Y* distances and warm colors stand for shots south of the fault. Figures 5b and 5e show the results at two stations aligned with the active source line within the barrier segment. Figures 5c–5e show the comparison in the along-strike direction (on the three different segments).

a poorer agreement at station G04. In particular, our model does not reproduce the full amplitude of the low-velocity anomaly suggested by the data. Based on the good fits along the rest of the fault (G06 and G08), this disagreement suggests that the wave speed beneath G04 may be slower than in the model in segment 3 (Figure 2, left). The overall agreement is satisfying in view of the amount of active data in the system (<10% of the absolute times data set) and confirms the main features of our along-strike fault zone V_p model (Figure 2).

4. Temporal Evolution of Fault-Zone *S* Velocities and Microseismicity

In view of the long-term mechanical behavior described by *McGuire* [2008] and *Boettcher and McGuire* [2009], the segmentation in velocity structure observed here suggests that the asperity area (around the 2008 M_w 6 epicenter) is associated with relatively higher *P* wave velocities (segment 2), whereas the barrier area is associated with lower *P* wave velocities (segment 1). The mechanical behavior of each segment can be further characterized by temporal changes in travel time and, thus, seismic velocity, which can be inferred from doublet events directly underneath stations within each segment (that is, G08, G06, and G04). We define doublets as events with similar waveforms and contained within a cluster ~3 km long in the along-strike direction. In practice, the velocity change is measured by comparing a reference trace, chosen as a stack of those similar waveforms, to each of individual waveform. We follow nearly the same procedure as in *McGuire et al.* [2012]. In particular, we use the so-called stretching technique [e.g., *Lobkis and Weaver*, 2003; *Sens-Schönfelder and Wegler*, 2006], which provides the overall delay, as an initialization of the doublet method [*Poupinet et al.*, 1984]. The latter has more precision for small changes and is used to refine the stretching measurement. However, our approach slightly differs from the one in *McGuire et al.* [2012]. We first use a global reference trace to measure the seismic velocity changes over the whole period. However,

©2014. American Geophysical Union. All Rights Reserved.

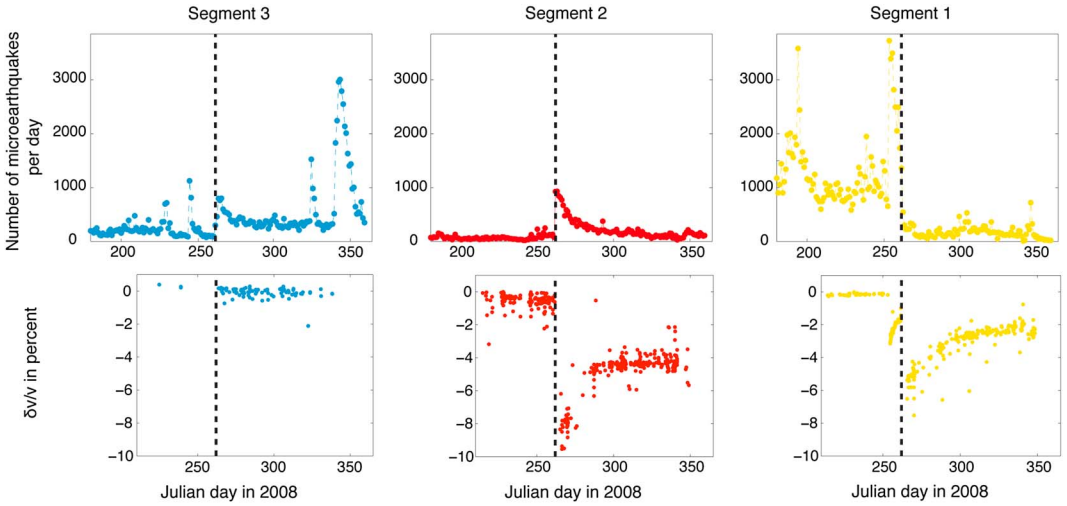

Figure 6. Temporal changes in (top) microseismicity rate and in (bottom) seismic velocity for the three segments. The vertical dashed line shows the time of the September M_w 6 event. The rate of microseismicity is taken from the waveform correlation detection catalog of *McGuire et al.* [2012], and has been estimated in 8 to 11 km long segments based on the along-strike V_p models (see Appendix B) for segments 1 and 2. As for segment 3, the rate of microseismicity shown corresponds to the entire western part of the fault beyond segment 2. The seismic velocity changes for segments 1, 2, and 3 come from changes in travel times between doublet seismograms recorded by G08, G06, and G04, respectively.

because of the large velocity variations occurring in the medium, this global reference may significantly differ from current waveforms, leading to noisy measurements. We thus perform measurements in four time periods to refine the temporal evolution locally. These four time periods are defined using the overall measurements and can be designated relative to the 2008 M_w 6.0 earthquake (which occurred on Julian day 262) as follows: the late interseismic period (Julian days 200–254), the preseismic period (Julian days 254–261), the early postseismic period (Julian days 263–290), and the late postseismic period (Julian days 290–365). Measurements within these periods are made using a "local" reference trace, that is, the stack of similar events within that time period. Within each of these time periods, we define similar events to be event clusters having waveform cross-correlation coefficients (cc) larger than 0.85. Note that the cc cutoff is lower and variable in the overall measurement to span the whole time range. We finally calculated the median value of the four periods using the overall measurement to put them on the same plot and estimate the amplitude of the major preseismic and coseismic changes. These measurements quantify changes in the average *S* wave velocity as seen by the first few seconds of the *S* wave coda. The changes are not simply mapped to a specific region within the Earth but given the frequency band used (~5–10 Hz) and the magnitude of the travel time delays, they likely represent an average over the shallow (~0–3 km) fault zone.

We also follow the temporal evolution of the microseismicity rate in each area. The latter has been estimated in 8 to 11 km long segments based on the V_p model (see Appendix B) for segments 1 and 2. As for segment 3, the rate of microseismicity shown corresponds to the entire western part of the fault beyond segment 2. This allows us to include the whole swarm of about 20,000 events that occur in December 2008 in the western part of the fault and extend into the area which is not resolved by our inversion according to the synthetic tests.

The temporal changes in shear wave propagation speeds and (micro)seismicity rates corroborate the along-strike segmentation of mechanical properties and seismogenesis (Figure 6). Segment 2, as depicted in Figure 6 (middle), shows a seismicity history dominated by aftershocks of the M_w 6 event that follow the typical Omori's law decay. The level of microseismicity before the main shock as well as a few weeks after is very low. The seismic velocity changes also show a strong signature of the M_w 6 earthquake with a clear coseismic velocity drop followed by at least a few weeks recovery. By contrast, segment 1 (Figure 6, right) shows a high level of microseismicity during the months before the M_w 6 event which culminates in an intense foreshock sequence in the week before the main shock. The seismicity dramatically drops at the time of the M_w 6 earthquake and remains very low in the postseismic period relative to the pre–main shock level. Seismicity rates clearly covary with changes in seismic velocity. This is most apparent before the main shock, when intensification of seismicity coincides with a clear reduction in seismic propagation speed (around Julian

©2014. American Geophysical Union. All Rights Reserved.

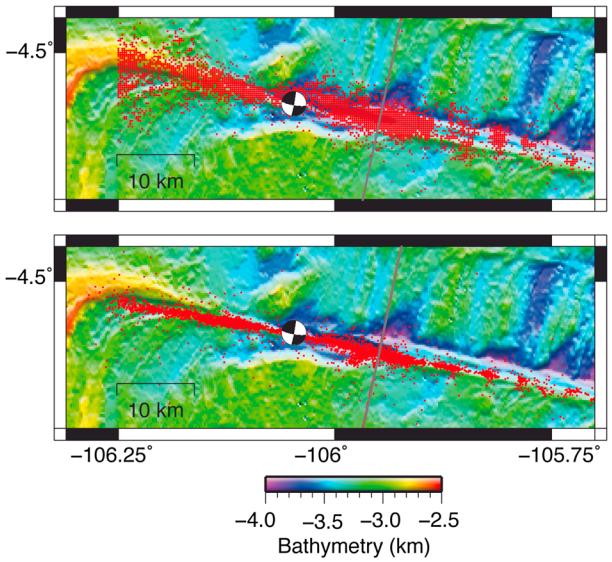

Figure 7. Comparison of the (top) initial location of the 7644 events (red dots) and the (bottom) relocation of 7391 of those events from the double difference approach (red dots). The 2008 M_w 6 earthquake is shown by its focal mechanism. The earthquake location has been estimated using a teleseismic surface wave cross-correlation technique in *McGuire* [2008]. As reference marker, the location of the active shot line is also displayed in dark gray.

day 254) (see *McGuire et al.* [2012] for details). In that segment, we also observe a strong coseismic velocity drop probably reflecting physical damage caused by coseismic strong ground motion from the M_w 6 event in a widespread area. In the western part of the fault (segment 3, Figure 6, left) we observe an increase of seismicity triggered by the M_w 6 earthquake. However, in contrast to segment 2, the level of seismicity remains high relative to the pre–main shock level. Seismicity near the end of the year (after day 340) is characterized by the above mentioned December swarm of about 20,000 events in the western fault. In this area, the seismic velocity changes are ambiguous because we did not find doublets spanning the entire time period, which prevents us from estimating a proper coseismic effect. The postseismic signature is, however, clearly different from the two other segments and shows no significant variation following the M_w 6 main shock. This suggests a weak signature of the earthquake, if any, probably reflecting the rupture extent and, considering the difference with segment 1, possibly main shock directivity toward the east.

Note that the temporal evolution of seismicity also highlights that the fault broke in a series of ruptures that propagated from east (segment 1 in the pre–main shock period) to West (segment 3 in the post main shock period). This sequence can be extended to earlier times by the 2007 M_w 6 earthquake in the eastern part of the fault (green ellipse in Figure 1). The short-term mechanical behavior reflected by the evolution of microseismicity confirms the strong differences between segments in that the main shock clearly triggered seismicity in segment 2 whereas it inhibited it in segment 1. Moreover, with the caveat that the model in segment 3 is associated with significantly higher uncertainties, Figures 2 and 6 together suggest that swarm segments (1 and 3) correspond to low V_p zones, supporting a direct link between the extent of the damage zone, as reflected by V_p and the way in which the fault ruptures.

5. Seismicity Location

The locations of microseismic events give insight into fault or fracture delineation. The double-difference approach allows us to improve the event location significantly, thanks to the use of the differential arrival times: whereas the initial locations from the STA-LTA catalog define a 3–4 km wide microseismic zone, it collapses to a width of ~400 m in some areas (Figures 7 and 8) after relocation. The relocated microseismicity outlines a nearly linear fault closely following its bathymetric expression (Figure 7). The western fault trace seems to branch into two subparallel segments (Figure 8, top). This feature must however be considered with caution considering its location at the edge of the network. Figure 8 also shows a bend that offsets the fault trace by about 600 m. Intriguingly, this structural complexity occurs near the boundary between segments 1 and 2. The influence of fault geometry on rupture dynamics has been studied for many years, and fault trace discontinuities are known to be critical in rupture initiation and termination [e.g., *King and Nábělek*, 1985; *Sibson*, 1985; *Wesnousky*, 2006]. The presence of this discontinuity therefore raises questions about the possible influence of geometric features on lateral rupture propagation on the Gofar fault. We will come back to this point in the discussion section.

Figure 8 (bottom) displays vertical slices of the location of microseismicity superimposed on the *P* wave velocity model. The along-strike depth extent of the relocated microseismic events emphasizes the same

©2014. American Geophysical Union. All Rights Reserved.

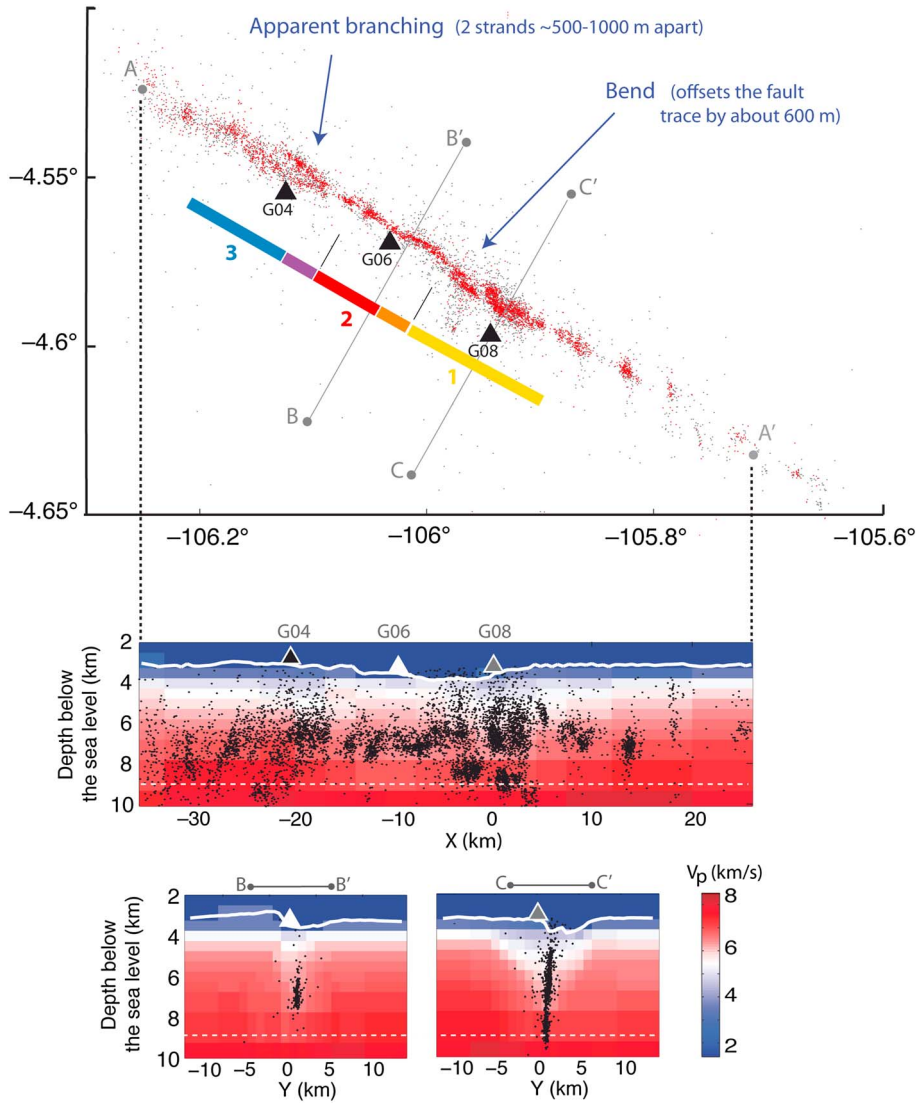

Figure 8. (top) Location of the 7391 (out of 7644) events relocated by the double-difference analysis. The red dots are 50% of events relocated with the most data. The gray dots are the remaining relocated events. The latitudinal axis has been exaggerated by 2.5X. The thick colored lines indicate segments 1, 2, and 3 as defined by our along-strike V_p models (Figure B2). As in Figure B2, purple and orange lines correspond to transition areas. (bottom) Cross sections AA′, BB′, and CC′ of the event locations (black dots) superimposed on the V_p model. The location of the cross sections is indicated in Figure 8 (top). Note that the velocity color scale is such that dark blue corresponds to the water column. The white solid line corresponds to the sea bottom in the central fault zone. The white dashed line highlights the depth of the Moho estimated by *Roland et al.* [2012] in the barrier area (i.e., beneath G08).

segmentation seen in the *P* wave velocity model. Indeed, in the fast segment 2, seismicity is contained within the intermediate oceanic crust (around 3–4 km below the sea bottom). This agrees well with the expectation from thermal models of oceanic crust. By contrast, seismicity in the swarm segments (1 and 3) covers a much larger depth range. This is another element pointing to the difference in physical properties of these segments. The two across-fault slices clearly show the delineation of the fault at depth. We can observe that the fault is nearly but not perfectly vertical (dip ~85–86°). Since the seismicity in the asperity area covers only a limited portion of the fault, we can notice that this slight tilt implies that the fault looks narrower in the map projection in Figure 8 (top).

Differential *S* wave travel times are very useful for constraining relative earthquake locations, but the use of absolute *S* wave data merits discussion. On one hand, the relatively low quality of these data justifies our initial decision not to use them in the inversions. On the other hand, their omission degrades seismic event location, especially hypocenter depth, making it more difficult to constrain the depth extent of the seismic

©2014. American Geophysical Union. All Rights Reserved.

zone. Perhaps as a result, our locations in the barrier area (that is, beneath G08) are systematically shallower than those obtained by *McGuire et al.* [2012] with the HypoDD algorithm [*Waldhauser and Ellsworth*, 2000], which uses a double-difference approach to seismic event relocation and (in contrast to TomoDD) a fixed velocity model. *McGuire et al.* [2012] used a 1-D version of the *P* wave velocity model of *Roland et al.* [2012], which accounts for the low velocity in the barrier fault zone. They argued that the large *S-P* travel times (up to ~1.25 s) observed at G08 for events located just beneath it require seismicity as deep as 8–9 km below the sea floor (assuming an ordinary V_p/V_s ratio for gabbro, that is, ~1.7), which for a Moho depth of ~5.5 km [*Roland et al.*, 2012] implies that some events occur in the uppermost mantle. TomoDD relocation without absolute *S* times yields maximum event depths between 6 and 7 km, that is, mostly within the crust (Figure 8, bottom). Oceanic earthquakes are generally confined to depths shallower than the 600°C isotherm [e.g., *Abercrombie and Ekstrom*, 2001; *Braunmiller and Nábělek*, 2008]. For thermal models that include hydrothermal cooling, this depth reaches ~5–6 km [*Roland et al.*, 2010]. Thus, the depth extent of seismicity found here is pretty consistent with these models while the deeper seismicity found by *McGuire et al.* [2012] in segment 1 is not. But our preferred model fails to explain the large *S-P* times and the absolute *S* wave travel times are poorly fit (Figure C1b in Appendix C). This is understandable since we downweight *S* times in the inversion scheme and even rule them out from the absolute data set. The large-scale *S* wave velocity model is then frozen in the tomoDD algorithm. This does not question the relevance of using the differential *S* wave travel times between nearby events which are basically not sensitive outside of the source region and can be useful to constrain the relative earthquake location.

To test the influence of the *S* wave data on our results we performed an inversion with the entire *S* wave data set (that is, including the absolute arrivals) using the same weight for *P* and *S* data. We will refer to this test as the *S + P run*. As expected, the resulting model produces a much better fit to *S* wave data for upgoing paths beneath G08 (Figure C1d in Appendix C), and it also provides a closer match to the observed *S-P* times. The resulting *P* wave velocity model is not satisfactory, however, because of the poor fit to the active source data (Figure C3). This is important because, as we mentioned before, the travel times from active source experiments only depend on the velocity model (the source locations are known). For our investigation of the V_p structure we, therefore, focus on the model which fits the active source wave data the best.

Figure C2 in Appendix C shows that the overall depth extent of seismicity does not change much, although the *S + P run* does yield locations in the upper mantle (See Appendix C for a more detailed discussion about the comparison between the two relocation results.) Instead of producing larger event depths (around 7–10 km below the sea floor as in *McGuire et al.* [2012] versus 6–7 km in this study) the *S + P run* maps the large *S-P* times into a fault zone V_p/V_s ratio between 2 and 2.5. This seems to be a bit inconsistent with *McGuire et al.* [2012] who estimated a V_p/V_s ratio close to normal (~1.7) for the lower crust. However, this ratio may differ throughout the crust, and if enhanced fluid-filled porosity occurs in segment 1 (see section 6) we may expect that the V_p/V_s ratio rises at least in some parts of the crust. To check the depth sensitivity of the data used, we performed inversions with initial event locations moved deeper by 2 km (Appendix D). The stability of the retrieved depths suggests that our system can converge to the same depth relocation, independent of initial locations. These tests suggest that using the *S* waves in the same way as *P* waves does not lead to very different depth locations. However, the *S + P run* shifts microseismicity laterally (but preserving the delineation), sending the seismicity clearly outside of the low-velocity fault zone revealed both by our model and the high-resolution model obtained by *Roland et al.* [2012]. The interrelation of V_p and V_s models through the event location may thus explain that poor quality *S* wave picks can therefore affect significantly the V_p model.

Despite the encouraging results of these test inversions, we take here the conservative view that the precise depth extent of the seismicity and the V_p/V_s ratio are not well constrained by the data used and that, especially, the continuation of seismicity into the upper mantle beneath G08 remains somewhat unclear. As agreed by *McGuire et al.* [2012], the V_p/V_s ratio may play a role in the large *S-P* times observed in segment 1, but these two studies show that we are not able to quantify unambiguously its impact yet and thus to conclude on the main process explaining the *S-P* observations. However, improving *S* wave picks could help resolve this question in future studies. Despite these uncertainties, however, the along-strike segmentation in seismicity and, in particular, the features highlighted in Figure 8 are robust. Furthermore, we have seen that the *S + P run* does not lead to a satisfactory V_p model, and the uncertainties in hypocenter depths do not challenge our conclusions about the velocity structure. First, our model is consistent with the model of *Roland et al.* [2012], which is based on a different tomographic method and a somewhat different data

©2014. American Geophysical Union. All Rights Reserved.

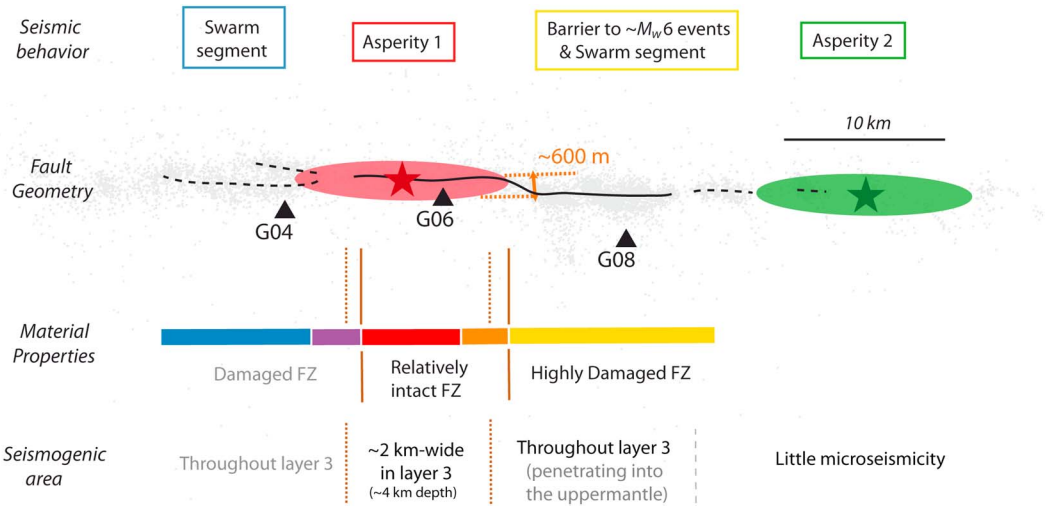

Figure 9. Summary cartoon of the main results. This cartoon synthesizes the information on the fault segmentation brought by different observables: (top, middle, and bottom) the overall mechanical behavior, the geometry and the material properties of the fault zone, and the seismogenic area as defined by the depth extent of the seismicity. The red and green ellipses are centered on the 2008 M_w 6.0 (red star) and 2007 M_w 6.2 (green star) earthquakes, respectively, and indicate two main asperities that break every 5 to 6 years. The thick colored lines indicate the different segments as defined by our along-strike V_p models (Figure B2). FZ stands for Fault Zone. Layer 3 refers to the usual oceanic crust nomenclature and basically designates gabbros. Gray text and gray dashed lines indicate observations which remain open to question because of the limited resolution of the model.

set. Indeed, they used active shot *P* and PmP arrival times, whereas active shot *P* times represent <10% of the absolute data set (and a very small part of the entire data set) used here. Second, the good fit to active data, especially in segments 1 and 2, supports the inferred transition from the rupture barrier to the asperity based on observations of large earthquake behavior throughout many seismic cycles at this fault, which is the main focus of this paper.

6. Discussion and Conclusions

The main results of this study concerning the Gofar fault segmentation are synthesized in Figure 9. Considering the much higher uncertainties associated with results in segment 3 revealed by the different resolution tests, we will focus in the following discussion on differences between segments 1 and 2.

The Gofar oceanic transform fault setting provides unique observations that cover more than four seismic cycles over 25 years [*McGuire*, 2008; *Boettcher and McGuire*, 2009]. Our imaging study indicates that the asperity region that breaks in ~M_w 6 earthquakes (repeatedly over several seismic cycles) coincides with a relatively high *P* wave velocity fault zone, whereas the barrier zone which stops moderate to large ruptures (repeatedly over several seismic cycles) and shows abundant microseismicity, is characterized by a low-velocity fault zone. Our velocity model suggests a ~8 km long asperity (Figure B2). Our study further reveals that this asperity is terminated to the east by a <1 km bend in the fault trace. It is worth noting that these main observations are strikingly consistent with what is observed just to the north, on the western part of the Discovery fault (4°S; 104.4°W). On this fault, *Wolfson-Schwehr et al.* [2014] use both high-resolution bathymetry and precise relocation of seismicity (including microseismicity and 15 > M_w 5.4 events) to explore the influence of the fault structure on the seismic behavior. As observed on Gofar as well as on other Pacific RTFs [e.g., *Sykes and Ekström*, 2012], they found distinct repeating rupture patches separated by regions that apparently do not support large ruptures. In particular, they identified a ~10 km long rupture patch that broke in 1996, 2001, and 2012 in ~M_w 6 events on the western part of the fault. Similarly to the Gofar asperity, this patch is confined by small-scale (bathymetric) features and surrounded by zones of low seismic coupling and high rates of microseismicity. These two studies support the idea that (i) these faults consist of segments of different geologic properties and (ii) small-scale complexities in the fault trace (<1 km) may play a role in controlling the rupture extent.

Roland et al. [2012] investigated the origin of the fault zone low velocities in the barrier area and discussed the potential contributions from porosity and mineral alteration. They conclude that (i) the volume of

©2014. American Geophysical Union. All Rights Reserved.

altered material (such as serpentinite) required to explain the low wave speeds in the barrier fault zone is incompatible with the local gravity field and (ii) high porosity, possibly reaching a few percent, is consistent with various geophysical observations and the most likely factor causing the low *P* wave velocities. The temporal evolution displayed in Figure 6 shows a seismic velocity decrease in segment 1 in the week preceding the September main shock. This decrease reflects a change in physical properties within the rupture barrier region. Subtle velocity changes during periods of earthquake activity have been observed at a wide array of regional seismogenic regions from local fault zones to regional fault systems [e.g., *Vidale and Li*, 2003; *Rubinstein and Beroza*, 2004; *Peng and Ben-Zion*, 2006; *Brenguier et al.*, 2008; *Froment et al.*, 2013] and are commonly associated with damage and/or static stress change. At the Gofar fault, it seems likely that the decrease in *S* wave velocity within segment 1 the week before the main shock is caused by damage during the intense foreshock sequence possibly associated with additional aseismic process [*Roland and McGuire*, 2009; *McGuire et al.*, 2012]. If microseismicity and aseismic creep facilitated an episode of fracture opening (consistent with the decrease in wave speed), increased porosity just before the main shock would make this zone prone to dilatant strengthening. Dilatant strengthening, that is related to the tendency for pore space to increase and therefore effective normal stress to decrease during stress episodes in highly porous media, may act to suppress dynamic slip within the rupture barrier region at the time of the main shock event [*Segall et al.*, 2010; *Segall and Bradley*, 2012]. Furthermore, with enhanced porosity, it is likely that some serpentinization has occurred, even if it is not the main explanation for the low velocities. Laboratory studies have shown that under certain stress and temperature conditions, serpentine minerals demonstrate velocity-strengthening behavior [*Reinen*, 2000; *Moore and Lockner*, 2007], which could promote stable sliding in segment 1. The impact of rupture dynamics on the behavior of segment 1 is further highlighted by the sudden cessation of seismicity at the onset of the M_w 6 earthquake (Figure 6).

The relocated epicenters reveal a bend that offsets the fault trace by ~600 m near the boundary between the main shock asperity and the rupture barrier (i.e., the border between segments 1 and 2 ; see Figure 8). Small-scale geometrical complexities have also been observed at the ends of rupture patches on the western Discovery fault [*Wolfson-Schwehr et al.*, 2014] raising the question of the role of such structural features in the segmentation of M_w 6 ruptures on EPR transform faults. Even though the discontinuity seen on Gofar is smaller than those typically observed to stop M_w 6 ruptures [*Lettis et al.*, 2002; *Wesnousky*, 2006], it may still perturb local rupture dynamics by reducing rupture velocity propagation. However, even if small discontinuities like this one terminate the M_w 6 ruptures, they would not explain the overall seismic slip deficit observed globally on RTFs [e.g., *Boettcher and Jordan*, 2004]. Some material property of the rupture barriers, beyond geometry, must prevent them from contributing to the global moment budget of RTFs. A connection may exist in that the geometrical complexities probably either contribute to and/or result from along-strike variations in the extent of damage within the fault zone. Zones of increased damage would be expected to have increased porosity and fluid flow, possibly allowing for widespread hydrothermal alteration that affects the ability of the fault zone to sustain large ruptures.

Approximately 75% of global plate motion on RTFs is not accommodated as major earthquakes and occurs aseismically [*Boettcher and Jordan*, 2004]. Our study gives some insight into the origin of this global earthquake deficit by revealing a clear correlation between the fault zone material properties and its mechanical behavior. In particular, we show an abrupt transition between a highly damaged low-velocity fault zone in the area devoid of large earthquakes and a nearly intact and significantly faster fault zone in the asperity area. Combined with previous studies of Gofar's seismic cycles, this observation leads to the suggestion that the global deficit in seismic moment on RTFs results from the typical segment of an RTF occurring within a wide, low-velocity, high-porosity damage zone with material properties that do not allow for a typical seismic cycle. This may result from either the frictional properties of altered minerals in the fault-zone or the inability of the damage zone to store the strain energy required for a robust seismic cycle. In contrast, the RTF fault segments occurring in relatively intact gabbro and peridotite would undergo typical cycles of stress buildup and release in earthquakes such as those seen in segment 2 [*McGuire*, 2008] and on the Clipperton Fault [*Van Avendonk et al.*, 1998, 2001]. It is worth noting that this model is very similar to observations of the Parkfield section of the San Andreas fault where the repeating M_w 6 rupture zone corresponds to a portion of the fault that juxtaposes intact high-velocity rocks on each side of the fault, compared with adjacent creeping zones with less competent rock on the northeast side of the fault [e.g., *Michael and Eberhart-Phillips*, 1991]. Overall, the along-strike variations in fault zone velocity structure found in our

©2014. American Geophysical Union. All Rights Reserved.

Table A1. Weighting Scheme Throughout the Inversion Procedure for Waveform Cross-Correlation Data (Columns 2–5) and Catalog Data (Columns 6–9)[a]

	Cross-Correlation Data				Catalog Data				
Iterations	*P* Wave Weight	*S* Wave Weight	Misfit Weight	Distance Weight	*P* wave Weight	*S* wave Weight	Misfit Weight	Distance Weight	Abs/Diff Ratio
1–5	0.01	0.01	-	-	0.1	0.08	7	-	10
6–10	0.01	0.01	-	-	1	0.8	7	-	0.1
11–15	1	1	7	2	0.01	0.008	7	-	0.1

[a]*P wave weight* and *S wave weight* stand for the a priori weight for both types of waves. The data are reweighted by multiplying these a priori quality weights based on the misfit from the previous iteration. (*Misfit Weight* is a residual cutoff, expressed as a factor of standard deviation), and/or on the offset between events (*Distance Weight*, in km). The last column gives the relative weighting between absolute and differential data.

study supports the conclusion that extended highly damaged zones are the key factor in limiting the global earthquake productivity of RTFs to be much less than that expected from plate motion.

Appendix A: Evolution of Inversion Parameters

To combine the three types of data (absolute arrival times, catalog, and WCC differential times) into one system, we apply a hierarchical weighting scheme during the inversion. We start the inversion by applying greater weight to the absolute times to establish the large-scale result (Iterations 1–5; see Table A1). Then the differential data are weighted more to refine the event locations and the velocity structure at smaller scale (Iterations 5–10). In the final stage (Iterations 10–15), the WCC data are then weighted even more than the catalog differential times to further refine the model near the source regions. Distance weighting is used in this final stage to control the maximum separation between event pairs and apply greater weight to pairs of closer events. Finally, we reweight the data throughout the inversion procedure according to misfit to reject or downweight observations with large residuals. Table A1 synthesizes the weighting scheme during the whole iteration process. Further details about these weighting parameters can be found in *Waldhauser and Ellsworth* [2000]. At the end of the procedure, we still have 94% of WCC observations and 76% of Catalog observations.

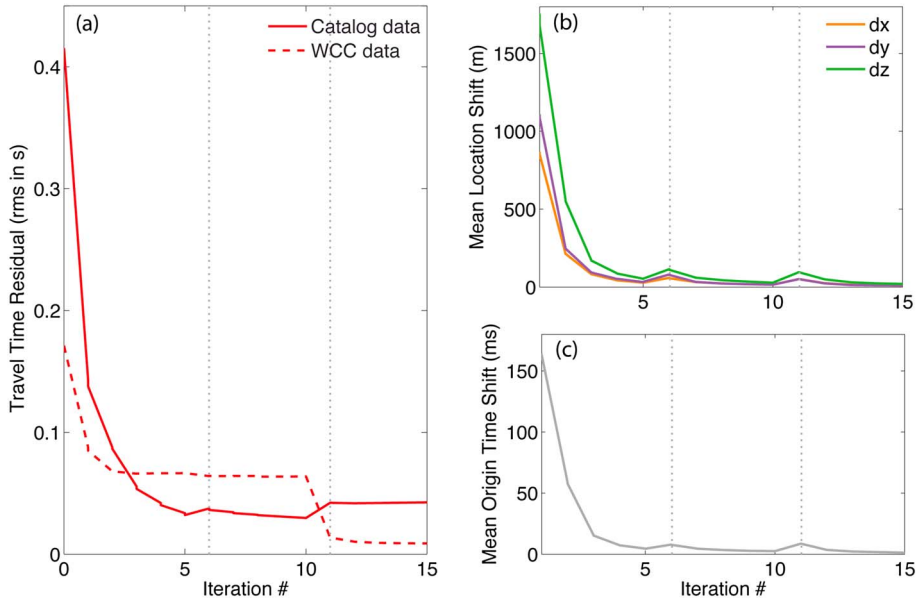

Figure A1. (a) Evolution of the root-mean-square travel time residuals for catalog and waveform cross-correlation (WCC) data, absolute values (b) of the mean hypocenter location shift in the three directions *x*, *y*, *z*, and (c) of the mean event origin time shift throughout the inversion procedure. The vertical dot lines at Iterations 6 and 11 indicate changes in weighting scheme regime (see Table A1).

©2014. American Geophysical Union. All Rights Reserved.

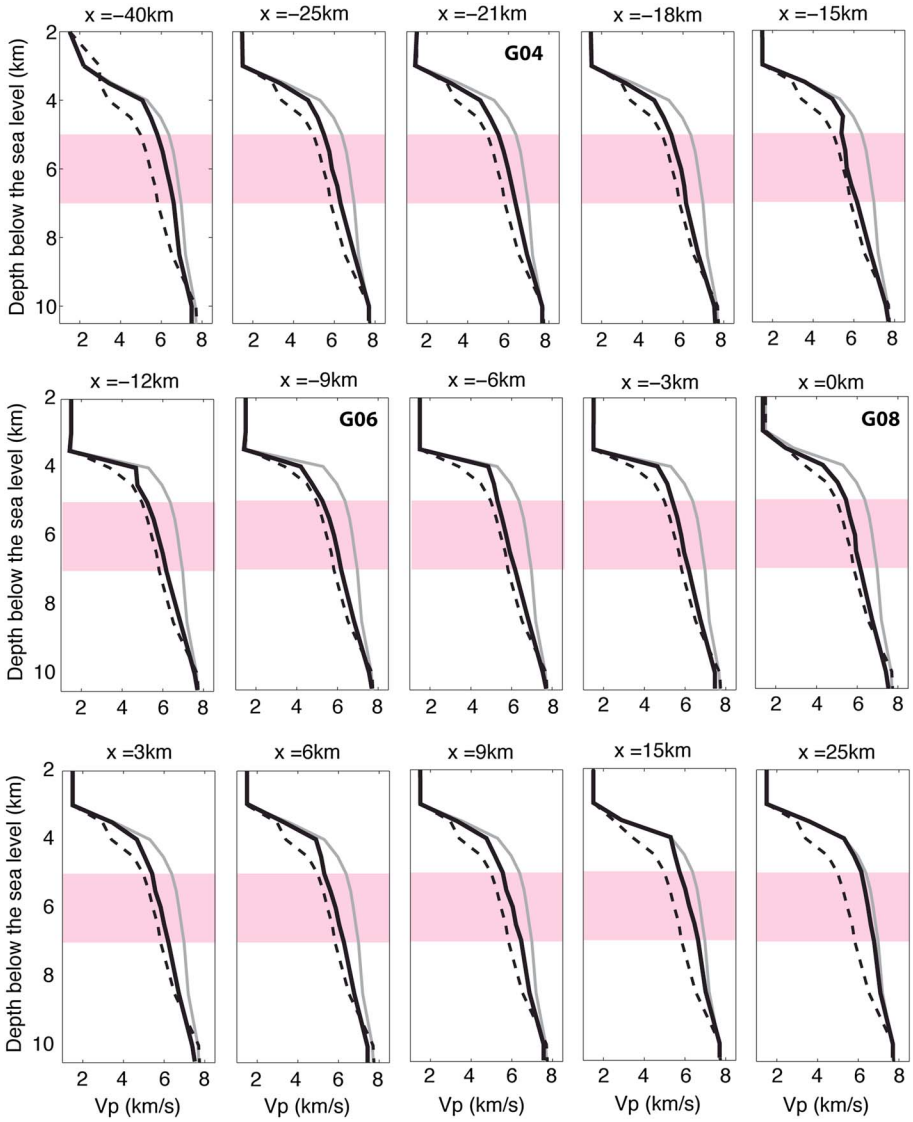

Figure B1. Along-strike synthetic tests. Each panel shows the V_p input model (black dashed line) used to build the synthetic data, the starting (gray curve), and resulting (black solid black line) models of the inversion of the synthetic data, at a given along-fault position x. In the ideal case, the black solid line should be exactly superimposed to the dashed line. The pink-shaded area shows the depth range used for the 10% criterion of resemblance between the input and the resulting model. Positions of stations G04, G06, and G08 are recalled for reference.

Figure A1 shows the (a) evolution of the travel time residual, (b) the mean hypocenter location change, and (c) the mean origin time change during the inversion. We observe that the model consistently converges toward stable results. Vertical dot lines at Iterations 6 and 11 indicate the change in weighting scheme regime (Table A1). This introduces momentary irregularities in the curves that quickly get back to converging solutions. The increase in catalog data misfit after Iteration 10 is caused by insertion of WCC data in the system. Note that these curves give the overall improvement of the model and show that the evolution is consistent throughout the procedure. They are however limited in reflecting the actual finer improvements due to the use of differential data and cannot be used extensively to set up the iteration scheme.

Appendix B: Supplementary Views of the Models

B1. Along-Strike Synthetic Tests

Figure B1 shows the results of the synthetic tests described in section 3.2 for the whole along-strike range. As mentioned in the main text, these synthetic tests show that the model slightly overestimates velocity

©2014. American Geophysical Union. All Rights Reserved.

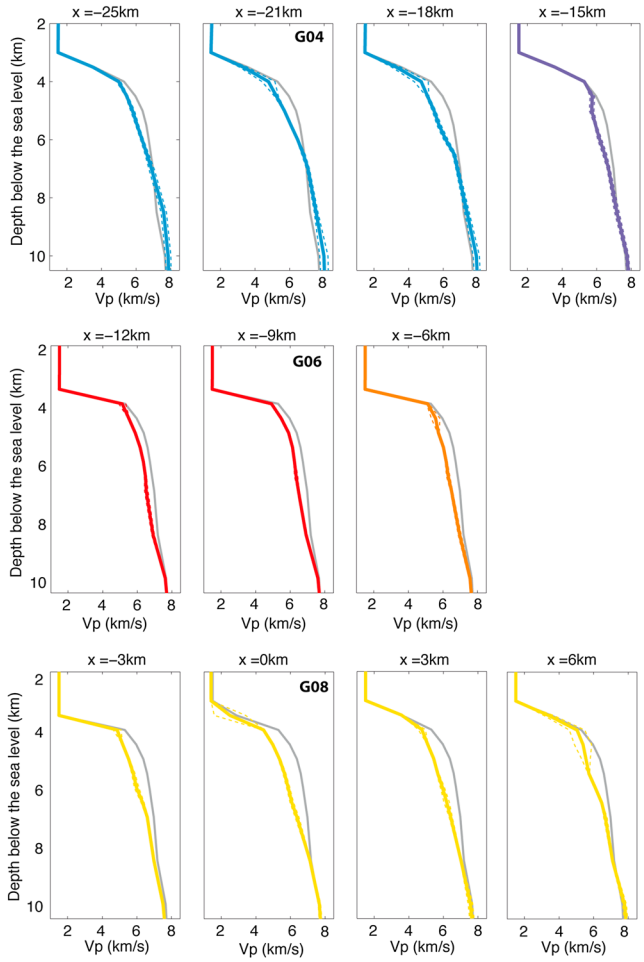

Figure B2. Along-strike variation in 1-D velocity-depth profiles (colored lines). The colors refer to the three segments discussed in the main body of the paper. Purple ($x = -15$ km) and orange ($x = -6$ km) curves are considered as transition zones. The dashed lines delimit the range of mean ± 1 standard deviation. The gray line stands for the starting model, representing normal EPR crust [*Roland et al.*, 2012]. Positions of stations G04, G06, and G08 are recalled for reference.

everywhere. The ray coverage thus prevents the system to fully retrieve the actual model from the relatively high-velocity starting model. These synthetic tests are used to determine the along-strike range we will consider for the rest of the paper. To do that, we consider the area for which the output model remains within 10% from the input model in the central part of the crust where the ray coverage is best (between 5 and 7 km below the sea level, pink-shaded area in Figure B1). The 10% threshold has been chosen based on the misfit at $x = 0$ (5 to 10%), where the ray coverage is expected to be the best (concentration of sources and receivers). This value is considered as a characteristic level of discrepancy and thus a lower limit for the rejection criterion. Based on that 10% criterion, we focused the interpretation on the −25 km to +6 km x range.

B2. Along-Strike 1-D Profiles

Figure B2 shows the along-strike variation in our P wave velocity model. This spans the range between $x = -25$ km and $x = 6$ km based on synthetic tests. This figure points out three clear distinct segments: a relatively normal EPR crust (around $x = -10$ km) surrounded by two slower zones (around $x = -20$ km and $x = 0$ km).

B3. Model Slices

Figure B3 shows the along-strike model in the center of the fault zone ((a)$y = 1$ km) and cross-fault models in the vicinity of (b) G04, (c G06), and (d) G08. The segmentation in the center of the fault again appears clearly from Figure B3a.

©2014. American Geophysical Union. All Rights Reserved.

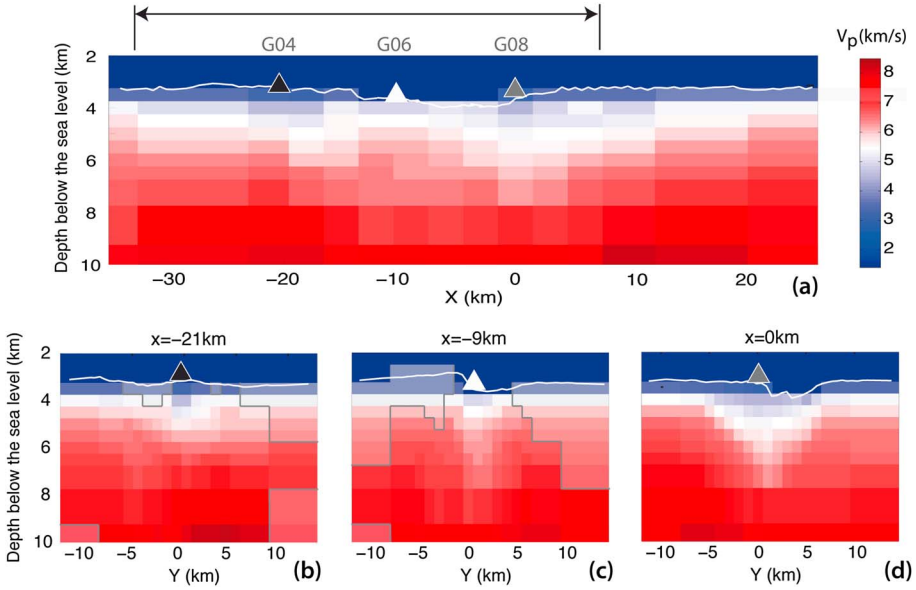

Figure B3. Slices of the *P* wave velocity model. (a) Along-strike model in the center of the fault zone ($y = 1$ km). Across-fault models in the vicinity of stations (b) G04, (c) G06, and (d) G08. Note that the velocity color scale is such that dark blue corresponds to the water column. The white solid line corresponds to the sea bottom. The double black arrow in Figure B3a indicates the along-strike range corresponding to satisfying synthetic tests (from Figure B1). The shaded area delimited by the gray line indicates the zone of the medium blank of any seismic rays.

Appendix C: Influence of *S* Waves

In order to estimate the influence of the *S* wave absolute time picks, we perform a test using the entire *S* wave data set with weights equals to the *P* wave ones. This *S* + *P* run helps explaining better both *P* and *S* wave travel times at G08 for upgoing paths (Figure C1). Figure C2 compares the relocation in depth of the seismicity for our preferred run and for the *S* + *P run*. These tests have been performed using the same inversion strategy. These two figures show that the overall relocation is fairly stable, especially if we look at the most reliable features highlighted by the events relocated with the most data (red dots). The seismicity seems to extend 1 km deeper in the *S* + *P* model sending some events into the upper mantle, but the

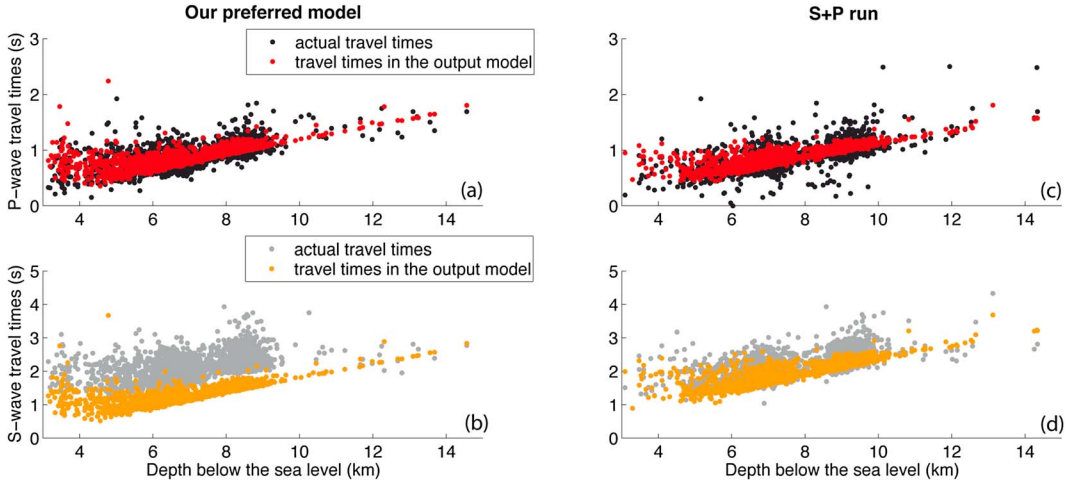

Figure C1. (top) *P* wave travel time data (black dots) and *P* wave travel times predicted by output models (red dots) at station G08 for events located beneath the station. The left and right columns represent results for our preferred run and the *S* + *P run*, respectively. (bottom) Similar for *S* wave travel time data (gray dots) and *S* wave travel times predicted by output models (orange dots). Note that some earthquakes are clearly located deeper than the main bulk of seismicity and may not be reliable.

©2014. American Geophysical Union. All Rights Reserved.

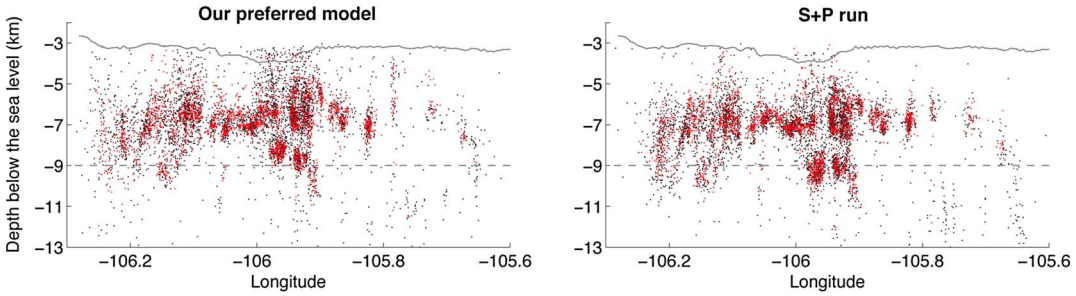

Figure C2. Along-strike versus depth relocation of the seismicity (left) for our preferred run and (right) for the *S + P run*. The red dots stand for the 50% of events relocated with the most data. The black dots stand for the other half. The gray solid line corresponds to the sea bottom in the central fault zone. The gray dashed line highlights the depth of the Moho estimated by *Roland et al.* [2012] in the barrier area.

seismicity remains within the first 7 km of the seafloor. This figure also brings to light a shallow cloud of scattered seismicity in our preferred model (some events being even located in the water). This cloud consists of events associated with very few data which confirms that this feature is not reliable and indicates that our model is not controlled by those events.

In terms of V_p model, we compared the fit to active data for both inversions. Figure C3 is the equivalent of Figure 5 for the *S + P run*. The fit in the barrier area (i.e., at G08 and G09) is quite similar to the one in our preferred model and even a bit better at G08. However, the fit at G09 is not as good, especially for southern (warm color) shots for which rays sample the low-velocity fault zone. The fit in other segments is significantly degraded and the *P* wave velocity model tends to be too slow. In particular, it fails to explain data at G06, that is, in the asperity area. The contrast in V_p between segments 1 and 2 of the fault zone being the main purpose of this paper, the *S + P run* fails to explain data related to this point.

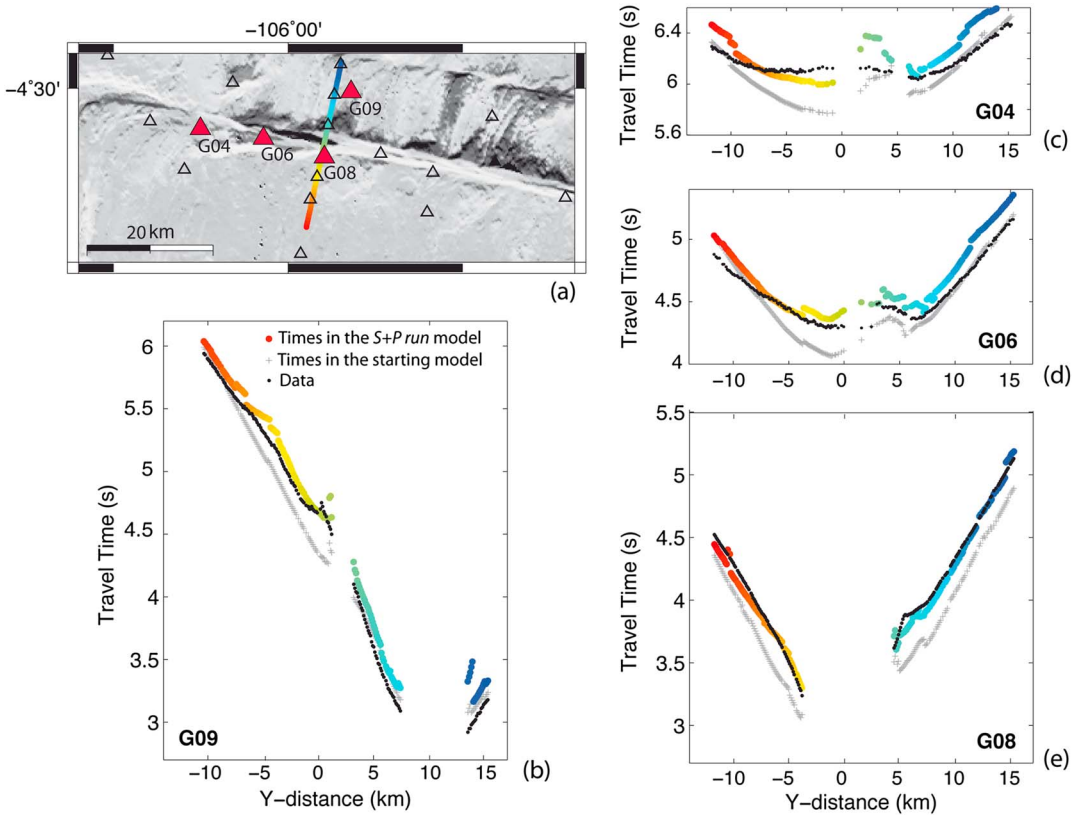

Figure C3. Similar to Figure 5 for the *S + P run*. Whereas the fit to the data is pretty similar in the barrier area (G08 and G09), it is significantly degraded off the active source line.

©2014. American Geophysical Union. All Rights Reserved.

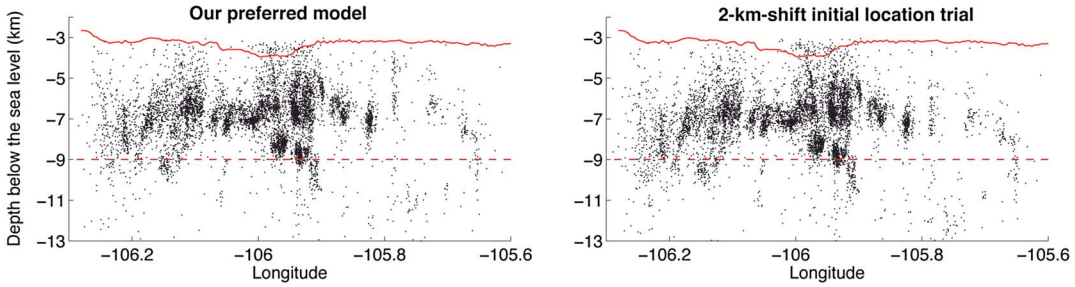

Figure D1. Along-strike versus depth relocation of the seismicity (left) for our preferred run and (right) for a similar run starting from event locations shifted 2 km deeper. The red solid line corresponds to the sea bottom in the central fault zone. The red dashed line highlights the depth of the Moho estimated by *Roland et al.* [2012] in the barrier area.

Appendix D: Influence of Initial Event Depths

We also tested the influence of the initial depth locations by starting the inversion with event locations shifted 2 km deeper. The relocation is remarkably stable (Figure D1). This test has been performed using the same inversion strategy as our preferred run. As for Figure C2, Figure D1 shows some fluctuations in relocation depth but the overall features are stable, and this figure does not show any significant seismicity beyond 7 km below the sea bottom.

Acknowledgments

All data used have been acquired and made available by WHOI. This data set is archived at the IRIS Data Center and publicly available to anyone. The material presented here is based on work supported by the National Science Foundation grants 1232725 and 0242117. We thank the W. M. Keck Foundation for the financial support to build the OBSs that carried strong-motion accelerometers. We thank Margaret Boettcher, Monica Wolfson-Schwehr, Harsha Bhat, Renata Dmowska for helpful discussions during the completion of this work as well as an Associate Editor and two anonymous reviewers who provide helpful comments and suggestions. We thank the crews of the RVs *Thomas G. Thompson*, *Marcus Langseth*, and *Atlantis* for three nearly flawless cruises needed to collect this data set. We thank the Woods Hole Oceanographic Institution (WHOI) Ocean Bottom Seismic Instrumentation Pool group, K. Peal, R. Handy, A. Gardner, D. Dubois, D. Kot, P. Lemmond, and J. Ryder, for collecting such an amazing data set.

References

Abercrombie, R. E., and G. Ekstrom (2001), Earthquake slip on oceanic transform faults, *Nature*, *410*(6824), 74–77, doi:10.1038/35065064.

Beroza, G. C., and S. Ide (2011), Slow earthquakes and nonvolcanic tremor, *Annu. Rev. Earth Planet. Sci.*, *39*, 271–296, doi:10.1146/annurev-earth-040809-152531.

Bird, P., Y. Y. Kagan, and D. D. Jackson (2002), Plate tectonics and earthquake potential of spreading ridges and oceanic transform faults, in *Plate Boundary Zones, Geodynamics Series*, vol. 30, edited by S. Stein and J. T. Freymueller, pp. 203–218, AGU, Washington, D. C.

Boettcher, M., and T. Jordan (2004), Earthquake scaling relations for mid-ocean ridge transform faults, *J. Geophys. Res.*, *109*, B12302, doi:10.1029/2004JB003110.

Boettcher, M. S., and J. J. McGuire (2009), Scaling relations for seismic cycles on mid-ocean ridge transform faults, *Geophys. Res. Lett.*, *36*, L21301, doi:10.1029/2009GL040115.

Braunmiller, J., and J. Nábělek (2008), Segmentation of the Blanco Transform Fault Zone from earthquake analysis: Complex tectonics of an oceanic transform fault, *J. Geophys. Res.*, *113*, B07108, doi:10.1029/2007JB005213.

Brenguier, F., M. Campillo, C. Hadziioannou, N. M. Shapiro, R. M. Nadeau, and E. Larose (2008), Postseismic relaxation along the San Andreas Fault at Parkfield from continuous seismological observations, *Science*, *321*(5895), 1478–1481, doi:10.1126/science.1160943.

Brune, J. (1968), Seismic moment, seismicity, and rate of slip along major fault zones, *J. Geophys. Res.*, *73*(2), 777–784, doi:10.1029/JB073i002p00777.

Detrick, R. S., R. S. White, and G. M. Purdy (1993), Crustal structure of North Atlantic fracture zones, *Rev. Geophys.*, *31*(4), 439–458, doi:10.1029/93RG01952.

Froment, B., M. Campillo, J. H. Chen, and Q. Y. Liu (2013), Deformation at depth associated with the 12 May 2008 MW 7.9 Wenchuan earthquake from seismic ambient noise monitoring, *Geophys. Res. Lett.*, *40*, 78–82, doi:10.1029/2012GL053995.

King, G., and J. Nábělek (1985), Role of fault bends in the initiation and termination of earthquake rupture, *Science*, *228*(4702), 984–987, doi:10.1126/science.228.4702.984.

Lettis, W., J. Bachhuber, R. Witter, C. Brankman, C. Randolph, A. Barka, W. Page, and A. Kaya (2002), Influence of releasing step-overs on surface fault rupture and fault segmentation: Examples from the 17 August 1999 Izmit earthquake on the North Anatolian Fault, Turkey, *Bull. Seismol. Soc. Am.*, *92*(1), 19–42, doi:10.1785/0120000808.

Lobkis, O. I., and R. L. Weaver (2003), Coda-wave interferometry in finite solids: Recovery of *P*-to-*S* conversion rates in an elastodynamic billiard, *Phys. Rev. Lett.*, *90*(25), 254,302, doi:10.1103/PhysRevLett.90.254302.

McGuire, J. J. (2008), Seismic cycles and earthquake predictability on East Pacific Rise transform faults, *Bull. Seismol. Soc. Am.*, *98*(3), 1067–1084, doi:10.1785/0120070154.

McGuire, J. J., J. A. Collins, P. Gouédard, E. Roland, D. Lizarralde, M. S. Boettcher, M. D. Behn, and R. D. van der Hilst (2012), Variations in earthquake rupture properties along the Gofar transform fault, East Pacific Rise, *Nat. Geosci.*, *5*(5), 336–341, doi:10.1038/ngeo1454.

Michael, A. J., and D. Eberhart-Phillips (1991), Relations among fault behavior, subsurface geology, and three-dimensional velocity models, *Science*, *253*(5020), 651–654, doi:10.1126/science.253.5020.651.

Moore, D. E., and D. A. Lockner (2007), Comparative deformation behavior of minerals in serpentinized ultramafic rock: Application to the slab-mantle interface in subduction zones, *Int. Geol. Rev.*, *49*(5), 401–415, doi:10.2747/0020-6814.49.5.401.

Peng, Z., and Y. Ben-Zion (2006), Temporal changes of shallow seismic velocity around the Karadere-Düzce branch of the North Anatolian Fault and strong ground motion, *Pure Appl. Geophys.*, *163*(2), 567–600, doi:10.1007/s00024-005-0034-6.

Poupinet, G., W. Ellsworth, and J. Frechet (1984), Monitoring velocity variations in the crust using earthquake doublets—An application to the Calaveras Fault, California, *J. Geophys. Res.*, *89*(NB7), 5719–5731, doi:10.1029/JB089iB07p05719.

Reinen, L. (2000), Seismic and aseismic slip indicators in serpentinite gouge, *Geology*, *28*(2), 135–138.

Roland, E., and J. J. McGuire (2009), Earthquake swarms on transform faults, *Geophys. J. Int.*, *178*(3), 1677–1690, doi:10.1111/j.1365-246X.2009.04214.x.

Roland, E., M. D. Behn, and G. Hirth (2010), Thermal-mechanical behavior of oceanic transform faults: Implications for the spatial distribution of seismicity, *Geochem. Geophys. Geosyst.*, *11*, Q07001, doi:10.1029/2010GC003034.

©2014. American Geophysical Union. All Rights Reserved.

Roland, E., D. Lizarralde, J. J. McGuire, and J. A. Collins (2012), Seismic velocity constraints on the material properties that control earthquake behavior at the Quebrada-Discovery-Gofar transform faults, East Pacific Rise, *J. Geophys. Res.*, *117*, B11102, doi:10.1029/2012JB009422.

Rubinstein, J. L., and G. C. Beroza (2004), Evidence for widespread nonlinear strong ground motion in the Mw 6.9 Loma Prieta earthquake, *Bull. Seismol. Soc. Am.*, *94*(5), 1595–1608, doi:10.1785/012004009.

Segall, P., and A. M. Bradley (2012), The role of thermal pressurization and dilatancy in controlling the rate of fault slip, *J. Appl. Mech.*, *79*(3), 031,013, doi:10.1115/1.4005896.

Segall, P., A. M. Rubin, A. M. Bradley, and J. R. Rice (2010), Dilatant strengthening as a mechanism for slow slip events, *J. Geophys. Res.*, *115*, B12305, doi:10.1029/2010JB007449.

Sens-Schönfelder, C., and U. Wegler (2006), Passive image interferometry and seasonal variations of seismic velocities at Merapi Volcano, Indonesia, *Geophys. Res. Lett.*, *33*, L21302, doi:10.1029/2006GL027797.

Sibson, R. H. (1985), Stopping of earthquake ruptures at dilational fault jogs, *Nature*, *316*(6025), 248–251, doi:10.1038/316248a0.

Sykes, L. R., and G. Ekström (2012), Earthquakes along Eltanin transform system, SE Pacific ocean: Fault segments characterized by strong and poor seismic coupling and implication for long-term earthquake prediction, *Geophys. J. Int.*, *188*(2), 421–434, doi:10.1111/j.1365-246X.2011.05284.x.

Tréhu, A. M., and G. M. Purdy (1984), Crustal structure in the Orozco transform zone, *J. Geophys. Res.*, *89*(B3), 1834–1842, doi:10.1029/JB089iB03p01834.

Van Avendonk, H. J. A., A. J. Harding, J. A. Orcutt, and J. S. McClain (1998), A two-dimensional tomographic study of the Clipperton transform fault, *J. Geophys. Res.*, *103*(B8), 17,885–17,899, doi:10.1029/98JB00904.

Van Avendonk, H. J. A., A. J. Harding, J. A. Orcutt, and J. S. McClain (2001), Contrast in crustal structure across the Clipperton transform fault from travel time tomography, *J. Geophys. Res.*, *106*(B6), 10,961–10,981, doi:10.1029/2000JB900459.

Vidale, J. E., and Y.-G. Li (2003), Damage to the shallow Landers fault from the nearby Hector Mine earthquake, *Nature*, *421*(6922), 524–526, doi:10.1038/nature01354.

Waldhauser, F., and W. Ellsworth (2000), A double-difference earthquake location algorithm: Method and application to the northern Hayward Fault, California, *Bull. Seismol. Soc. Am.*, *90*(6), 1353–1368, doi:10.1785/0120000006.

Waldhauser, F., and W. L. Ellsworth (2002), Fault structure and mechanics of the Hayward Fault, California, from double-difference earthquake locations, *J. Geophys. Res.*, *107*(B3), 2054, doi:10.1029/2000JB000084.

Wesnousky, S. G. (2006), Predicting the endpoints of earthquake ruptures, *Nature*, *444*(7117), 358–360, doi:10.1038/nature05275.

Wolfson-Schwehr, M., M. S. Boettcher, J. J. McGuire, and J. A. Collins (2014), The relationship between seismicity and fault structure on the Discovery transform fault, East Pacific Rise, *Geochem. Geophys. Geosyst.*, *15*, doi:10.1002/2014GC005445.

Zhang, H., and C. Thurber (2003), Double-difference tomography: The method and its application to the Hayward Fault, California, *Bull. Seismol. Soc. Am.*, *93*(5), 1875–1889, doi:10.1785/0120020190.

Zhang, H., and C. Thurber (2006), Development and applications of double-difference seismic tomography, *Pure Appl. Geophys.*, *163*(2–3), 373–403, doi:10.1007/s00024-005-0021-y.

©2014. American Geophysical Union. All Rights Reserved.